PAPER

Check for updates

Electrochemical synthesis of hydroxyl group-functionalized PProDOT/ZnO for an ultraviolet photodetector†

Zulpikar Helil,[a] Tursun Abdiryim, [ID] *[a] Ruxangul Jamal,[b] Aygul Kadir,[b] Yuzhu Che,[a] Dongna Zou[a] and Mariyam Niyaz[a]

Ultraviolet (UV) detectors based on zinc oxide (ZnO) nanorods (NRs) are ideal materials for UV radiation detection. However, owing to the surface effect of ZnO NRs, their speed of photoresponse and photosensitivity need to be improved. In this study, a UV photodetector was fabricated *via* electrochemical coating of poly(3,4-propylenedioxythiophene) grafted with functional groups (−OH) on a hydrothermally grown ZnO NRs. For comparison, poly(3,4-propylenedioxythiophene)/ZnO composites were synthesized using the same method. The structure of the composite film was characterized by Fourier transform infrared spectroscopy (FT-IR), UV-visible spectroscopy (UV-vis), X-ray diffraction (XRD), Raman spectroscopy (Raman), X-ray photoelectron spectroscopy (XPS), scanning electron microscopy (SEM), and energy dispersive X-ray spectroscopy (EDS). The effect of the polymer structure on the UV sensing ability of ZnO NRs was evaluated by fabricating a UV detector with a composite material. The structural results indicated that the PProDOT-type conductive polymer and ZnO composites were successfully synthesized. The UV photodetection results showed that the presence of functional groups (−OH) in polymer chains could enhance the responsivity of the material. The response time of the ZnO/PProDOT−OH composite was 15 s shorter than that of the ZnO/PProDOT composite. A rise in photocurrent induced an increase from 2.5 A W^{-1} to 34.75 A W^{-1} in the UV photoresponsivity of the ZnO/PProDOT−OH composite, compared with that of the pure ZnO NRs. The external quantum efficiency and detectivity significantly improved, the increases of which were attributed to the coupling of the polymer and ZnO NRs.

1. Introduction

Ultraviolet (UV) detection has been widely used in various fields, such as solar concealment, environmental monitoring, and chemical analysis.[1–3] Many broadband-gap nanomaterials, including GaN,[4] diamond,[5] ZnS,[6,7] MoS_2,[8,9] and $K_2Nb_8O_{21}$ (ref. 10 and 11) have been used in UV detection. Compared with the aforementioned materials, ZnO is the one preferred for UV photodetection because of its distinct characteristics, such as a direct energy bandgap (3.37 eV), n-type semiconductor behavior, and exciton binding energy reaching 60 meV at room temperature.[12,13] Therefore, ZnO has drawn considerable interest and shows potential as an ideal material for the fabrication of UV detectors.[14–18]

[a]Key Laboratory of Energy Materials Chemistry, Ministry of Education, Key Laboratory of Advanced Functional Materials, Autonomous Region, Institute of Applied Chemistry, College of Chemistry, Xinjiang University, Urumqi 830046, P. R. China. E-mail: tursunabdir@sina.com.cn

[b]Key Laboratory of Oil and Gas Fine Chemicals, Ministry of Education, Xinjiang Uygur Autonomous Region, Xinjiang University, Urumqi 830046, P. R. China

† Electronic supplementary information (ESI) available. See DOI: 10.1039/d1ra01962g

ZnO belongs to the wurtzite family and has a hexagonal crystal structure.[19] Its structure can be simply described as numerous closely arranged O^{2-} and Zn^{2+} layers alternately stacked along the *c* axis, and adjacent O^{2-} and Zn^{2+} form a tetrahedral structure.[20] ZnO exhibits a noncentral symmetry mainly due to its tetrahedral structure, which provides its distinct piezoelectric and thermoelectric properties.[21] The bandgap and band position of ZnO are similar to those of TiO_2, and its low valence band endows photogenic holes with strong oxidation capacity.[22] Moreover, one-dimensional ZnO nanomaterials usually have large specific surface areas, hence their superior optical absorption ability. Single-crystal one-dimensional ZnO nanomaterials have a charge transfer efficiency usually several orders of magnitude higher than that of polycrystalline materials,[23] ZnO exhibits electron mobility dozens of times higher than that of TiO_2.

A one-dimensional wide-band-gap ZnO NRs provides several advantages, including low reflectivity, high UV photon absorption, and charge-oriented transmission. It is an ideal material for constructing self-driven UV detection devices. The current optical response speed and photosensitivity of UV detectors fabricated from one-dimensional ZnO nanomaterials need to be

improved. To improve the sensitivity and response speed of UV photodetectors based on ZnO nanostructures, numerous studies have been conducted, including the formation of junctions with other wide-band-gap semiconductors, surface modification with conductive polymers, inorganic nanoparticles, and organic materials, and others.[24–29] Liao *et al.*[30] reported on self-driven visible-blind UV photodetectors based on n-ZnO nanowire and p-GaN thin-film composite heterojunctions. The device has ultrafast response rise time (~20 μs) and decay time (~219 μs) and responds considerably faster relative to pure ZnO photodetectors.

With their highly delocalized π ring electronic systems, conductive polymers exhibit strong optical absorption and thus are widely used in the manufacture of low-cost photoelectric sensors. Many photoresist polymers have been used in the modification of semiconductor metal oxides or sulfides to induce or enhance their photosensitivity. Polymers can improve the electron–hole separation of inorganic semiconductor materials. Wang *et al.*[31] prepared a zinc oxide nanoribbon UV detector. A ZnO surface coated with sodium polystyrene sulfonate (PSS) increases its photosensitivity by 5 orders of magnitude. Yang *et al.*[32] combined ZnO with polyaniline (PANI) and designed a sandwich-structured UV detector of a p–n type, with the p-type PANI as an intermediate layer. When UV light hits the ZnO side, the p–n junction on the other side can attract the photogenerated electrons *via* the external circuit, achieving a zero-bias response. Nakano *et al.*[33] presented ZnO NRs and poly(3,4-ethylenedioxythiophene PEDOT:PSS) composites as UV light detectors. The device can achieve a zero-bias light response, the responsivity under 370 nm UV light irradiation was 0.3 A W^{-1}. Poly(3,4-malondithiophene) (PProDOT), as a derivative of PEDOT, shows better electrochemical and processing properties than those of PEDOT.[34] In the study by Sun *et al.*, ZnO nanoparticle arrays exhibiting physical adsorption on the surface of water molecules can produce oxygen vacancy and defects and further affect the apparent photocurrent and characterization of PL. Le *et al.* showed that under plasma exposure, nitrogen (N)-doped ZnO NRs effectively induce relative chemical bonds between oxygen atoms and zinc atoms. Yuan *et al.* proposed that the gaseous dopant N$_2$O on ZnO nanowire can compensate the intrinsic donor defects, thus achieving controllable electronic transmission.[35] Therefore, PProDOT grafted with the OH functional group can be used to prepare improved polymer-modified semiconductor composite materials *via* the synergistic interaction between the functional group and ZnO. In most studies, ZnO NRs are coated with a polymer material by spin-coating or chemical *in situ* polymerization. This method is time-consuming and can hardly ensure the uniformity of polymer coating on the surface of ZnO NRs, affecting the light response of the device.

In the present study, we electrodeposited PProDOT onto ZnO nanoarrays grown hydrothermally to fabricate p–n type UV light detectors. ZnO/PProDOT–OH composites were prepared using the same technique to evaluate the effects of various polymers on the UV response of the ZnO NRs. The synergistic effect of the polymer and ZnO inhibited the recombination of photogenerated electrons on the ZnO surface, improving the optical

response of the device. Compared with UV detection devices fabricated from pure ZnO NRs, those produced from polymer and ZnO composites have shorter photocurrent rise and decay times and better UV detection performance. The surface of ZnO NRs was modified by grafting PProDOT with hydroxyl groups (–OH) to verify the influence of hydroxyl functional groups on the UV response of ZnO NRs.

2. Experimental

2.1. Reagents

3,4-Propylenedioxythiophene (ProDOT, >99%), zinc nitrate hexahydrate (Zn(NO$_3$)$_2$·6H$_2$O), zinc acetate dihydrate ((CH$_3$COO)$_2$ Zn·2H$_2$O), and hexamethylenetetramine were supplied by Shanghai Aldrich Company (Shanghai, China) and used as received. All chemicals used in the experiment were of analytical grade, and all aqueous solutions were secondary distilled water. Fluorine-doped tin oxide (FTO)-conductive glass was prepared by Japan Sheet Glass Co., Ltd., and isopropanol was prepared by Tianjin Yongda Chemical Reagent Co., Ltd.

2.2. Preparation of ZnO NRs

ZnO NRs were prepared following the hydrothermal method used in the literature.[36] The seed crystal layer of ZnO NRs was fabricated using the sol–gel technique. The seed solution was synthesized by dissolving zinc acetate dihydrate (CH$_3$COO)$_2$ Zn·2H$_2$O, (25 mM) in isopropanol. The prepared seed crystal solution was spin-coated on the cleaned FTO substrate. The seed layer was then annealed in a muffle furnace for 1 h to form a ZnO nucleation site. An aqueous solution for ZnO growth was prepared with 25 mM hexamethylenetetramine and 25 mM zinc nitrate. A piece of FTO substrate with the ZnO seed layer was placed at an angle against the wall of the autoclave with the conducting side facing down. The autoclave was sealed and placed in an oven at 95 °C for 4 h before the sample was rinsed with deionized water.

2.3. Monomer synthesis

The monomer ProDOT was purchased from Shanghai Aldrich Company (Shanghai, China) and used as received without further purification. The PProDOT–OH monomer was synthesized using a method reported in the literature.[37] 2,2-Bis(bromomethyl)propane-1,3-diol (11 g, 42 mmol) and DMOT (3 g, 21 mmol) were used as reactants, and 200 mL of toluene and *p*-TSA (0.4 g, 2.1 mmol) were used as a solvent and a catalyst. The mixture was stirred in a nitrogen atmosphere at 110 °C for 36 h. The reaction products were then naturally cooled to room temperature and rinsed with distilled water. The solvent was ultimately evaporated and purified by *n*-hexane and dichloromethane = 3 : 2 silica gel column chromatography. The white crystal was ProDOT-2CH$_2$Br.

ProDOT-2CH$_2$Br (2.0 g, 5.84 mmol), propionic acid (1.31 mL, 8.76 mmol), potassium carbonate (2.92 g, 23.4 mmol) and *N,N*-dimethylformamide (DMF, 20 mL) were mixed into a 50 mL flask and refluxed at 100 °C for 16 h. The brown liquid obtained from a previous procedure was extracted several times with

dichloromethane. It was then washed with distilled water numerous times and then dried with MgSO$_4$. The solvent inside was then removed by rotary evaporation. Purification by *n*-hexane and dichloromethane = 3 : 2 silica gel column chromatography was performed, and a yellow transparent liquid was obtained (ProDOT-2CH$_2$OCOC$_2$H$_5$). Subsequently, 2 mL of 3 M KOH (H$_2$O : CH$_3$CH$_2$OH = 1 : 1) and 2 mL of 0.272 M ProDOT-2CH$_2$OCOC$_2$H$_5$ (THF) was dropped into a flask, which was then heated to 60 °C. The temperature was held constant for 24 h. The reaction products were naturally cooled to room temperature and neutralized with saturated hydrochloric acid, extracted with dichloromethane, and dried with MgSO$_4$. The solvent was then removed by rotary evaporation, and the white powder was purified by column chromatography.

2.4. Preparation of the ZnO/PProDOT and ZnO/PProDOT–OH composites

ZnO NRs were prepared using the hydrothermal method on the FTO substrate, and ProDOT was electropolymerized on the ZnO NRs using CV mode. A solution of 0.01 M ProDOT and 0.05 M tetra-*n*-butylammonium hexafluorophosphate TBAPF$_6$ as electrolyte in dichloromethane solution were prepared. The electropolymerization synthesis was carried out using an electrochemical instrument (CHI660) and a three-electrode electrochemical cell in which working, counter and reference electrodes were ZnO NRs, a platinum electrode and Ag/AgCl, respectively. In the CV mode, the voltage range was 0–2 V with 100 mV s^{-1} sweeping rate for five cycles. A thin layer of PProDOT was subsequently formed on the ZnO NRs to produce ZnO/PProDOT composites. The ZnO/PProDOT–OH composite was synthesized using the same method. The prepared ZnO/PProDOT and ZnO/PProDOT–OH composites were then rinsed with dichloromethane.

2.5. Fabrication of the ultraviolet photodetectors

A schematic of the preparation of UV detectors from ZnO/PProDOT and ZnO/PProDOT–OH composite materials is presented in Fig. 1. A piece of ZnO NRs and another piece of polymer-grown ZnO NRs are attached back to back to prepare our composite-based UV detector. The photoresponse and current–voltage (*I*–*V*) characteristics of the devices were measured with an electrochemical instrument (CHI660) under UV illumination at λ = 365 nm wavelength, and the light intensity was 0.4 mW cm^{-2} produced using a ZF-20A dark box four UV analyzer which provided by Shanghai Yuezhong Instrument and Equipment Co., Ltd.

2.6. Characterization and instruments

The morphologies of the ZnO NRs and the ZnO/PProDOT and ZnO/PProDOT–OH composites were characterized by scanning electron microscopy (SEM, SO8010, Japan) with elemental mapping. The crystal structure of the samples was characterized by X-ray diffraction (XRD) using the Bruker D8 Advance diffractometer. The Fourier transform infrared (FT-IR) spectra of the samples were recorded using an FT-IR spectrometer (BRUKER-QEUINOX-55). Raman spectroscopy of the materials
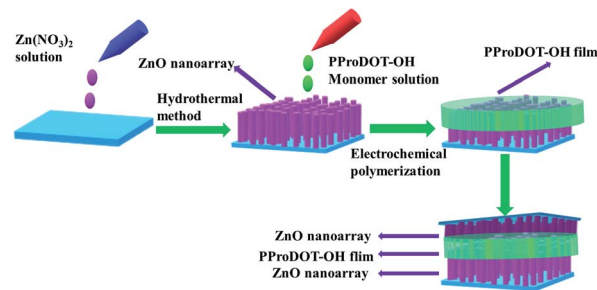

Fig. 1 Schematic diagram of preparation of UV detector.

was performed using the Bruker Vertex 70 FT Infrared Spectrometer. The transparency levels of electrodes and devices were measured by UV-vis spectrophotometry (UV4802, Unico, United States). The element content and chemical states of the ZnO, ZnO/PProDOT and ZnO/PProDOT–OH composites were characterized by X-ray photoelectron spectroscopy (XPS).

3. Results and discussion

3.1. Preparation of the ZnO NRs

Fig. 2(a) presents the top view scanning electron microscope image of the ZnO NRs. As shown in the figure, the nanoarrays exhibit high film density and uniform distribution on the FTO substrate. The nanoarrays are also well-aligned perpendicular to the substrate. In the inset in Fig. 2(a), the end face of the ZnO NRs appears as a hexagonal structure. The cross-sectional view in Fig. 2(d) shows that the ZnO NRs is continuous and grows at a relatively high density. The experimental results reported by Y.
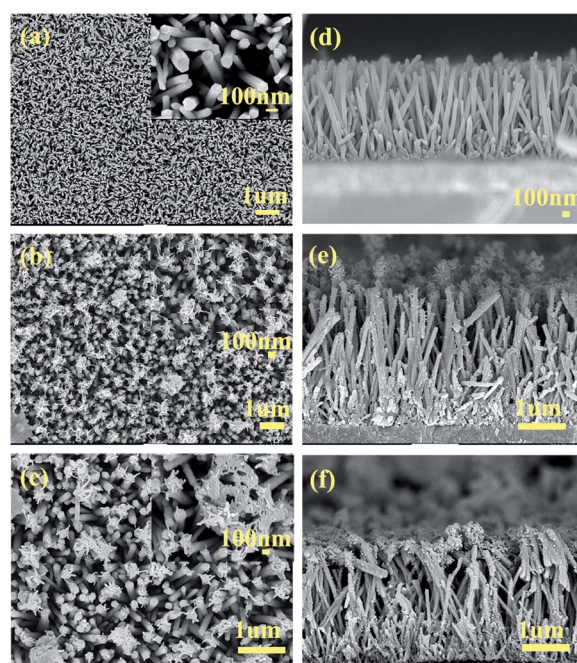

Fig. 2 Top-view SEM images of (a) ZnO (b) ZnO/PProDOT, (c) ZnO/PProDOT–OH, cross-sectional SEM images of (d) ZnO, (e) ZnO/PProDOT, (f) ZnO/PProDOT–OH.

C. Yoon *et al.*[36] showed that the structure of the seed layer determined the growth direction of growing ZnO nanowires. The growth direction of growing ZnO nanowires was controlled by Zn sputtering to produce a seed layer with different crystal ZnO nanowires. They also performed XRD phase analysis of the ZnO nanowires to determine the vertical arrangement and structural information of ZnO NRs. As can be seen from Fig. 2(b), (c), (e) and (f) PProDOT and PProDOT–OH polymer have been successfully electrodeposited on the ZnO NRs, and it can also be found that the morphology of the PProDOT and PProDOT–OH polymer films on the ZnO NRs is different. As shown in the Fig. 2(e), the average diameter of ZnO NRs electrodeposited by PProDOT increases with the polymerization of ProDOT monomer, and a thicker ZnO/PProDOT composite material was obtained, which indicates that ProDOT monomer can grow not only to the end surface of ZnO NRs but also to the outer surface of ZnO NRs when growing onto ZnO NRs. However, PProDOT–OH electrodeposited on ZnO NRs presents a fibrous shape, and PProDOT–OH will also grow on the upper end and outer surface of ZnO NRs, but the amount of PProDOT–OH polymer growing on the outer surface is less, and mainly grown onto the upper end surface of ZnO NRs in a fibrous shape.

3.2. Preparation of the ZnO/PProDOT, ZnO/PProDOT–OH composites

The monomers were electropolymerized by electropotential synthesis (*i.e.*, cyclic voltammetry). Polymer formation occurred after polymerization, as indicated by a change in color to blue. Fig. 3(a)–(d) are the linear scan and cyclic voltammetry curves of ProDOT and ProDOT–OH monomers electrodeposited on ZnO NRs, respectively. Fig. 3(b) illustrates the electropotential synthesis of ProDOT on ZnO NRs in a dichloromethane solution containing TBAPF$_6$ as the supporting electrolyte. In this study, the polymerization potential was scanned from 0 V to 2 V. As shown in the first cyclic voltammetry curve, the anode current begins to increase near 1.40 V, which is attributed to the oxidation of the ProDOT monomer. A loop appears in the first cycle of the current voltage characteristic of the result, caused by polymer nucleation.[38] The current rise in the first cycle indicates monomer ProDOT oxidation on the electrode, which starts at relatively higher potentials; in further cycles, the oxidation potential decreases by chain propagation.[39] In the current study, as the number of cycles increased, the oxidation potential decreased, indicating that the polymer exhibited higher electrical activity than that of ZnO NRs. In addition, the anode and cathode current strength increased with a rise in the number of cycles. This behavior can be explained by the growth of the conductive polymer on the surface of ZnO NRs.[40] As the number of cycles increases, the thickness of the conductive polymer film on the surface of ZnO NRs increases, indirectly increasing the number of rechargeable oxidation recovery origin on the surface of ZnO NRs.[41]

3.3. Redox behavior

Fig. S1† presents the cyclic voltammograms of electrodes in a solution of 1 M tetra-*n*-butylammonium hexafluorophosphate

in dichloromethane by scanning from −1.5 V to 1.5 V. ZnO, ZnO/PProDOT, and ZnO/PProDOT–OH composite electrodes were measured at scanning rates of 100 mV s^{-1}. No significant difference between the ZnO/polymer electrodes was found. The cyclic voltammetry windows of ZnO/PProDOT and ZnO/PProDOT–OH composite electrodes showed no significant differences at a scanning rate of 100 mV s^{-1}, indicating that the ZnO/polymer composites exhibited sufficient electrochemical activity.

3.4. Impedance analysis

Electrochemical impedance spectroscopy is a powerful tool for analyzing the conductivity of composite materials. The impedance spectra of the ZnO, ZnO/PProDOT, and ZnO/PProDOT–OH composite electrodes are presented in Fig. S2.† The diameter of the semicircle in the spectra denotes the charge-transfer resistance (R_{ct}) and double layer capacitance.[42] As shown in the Fig. S2,† the charge transfer resistance (R_{ct}) value of ZnO is the highest, followed by that of ZnO/PProDOT composite, and the RCT value of ZnO/PProDOT–OH is the lowest. Hence, the order of electrical conductivity performances are as follows: ZnO/PProDOT–OH > ZnO/PProDOT > ZnO. The introduction of a polymer layer reduces the charge transfer resistance (R_{ct}) values of pure ZnO because the conductivity of the polymer is higher than that of ZnO; moreover, the electrical conductivity of the composite material is improved after the deposition of polymers on the surface of ZnO. Under similar conditions, the charge-transfer resistance (R_{ct}) of the prepared ZnO/PProDOT–OH composite electrode is lower than that of ZnO/PProDOT. This difference indicates that the electrical conductivity of the ZnO/PProDOT–OH composite is higher than that of the ZnO/PProDOT composite, which is beneficial to improve the photoelectric performance of the composite material.

3.5. Ultraviolet-visible spectra

The UV-vis spectra of ZnO, PProDOT, PProDOT–OH, ZnO/PProDOT, and ZnO/PProDOT–OH composites are presented in
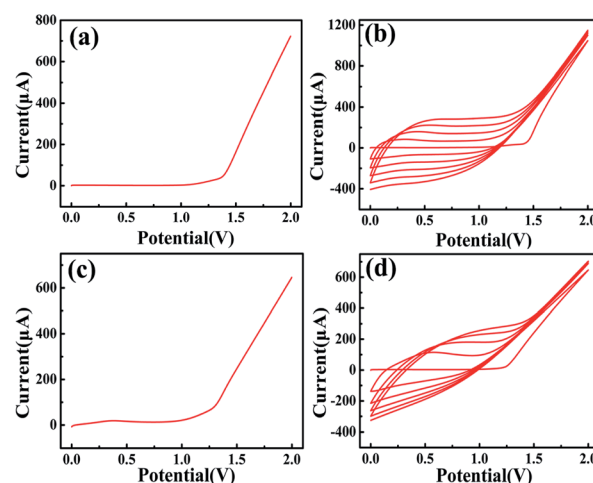

Fig. 3 The voltammograms of (a and b) ProDOT and (c and d) PProDOT–OH polymerization on ZnO NRs in an electrolyte of 0.05 M tetra-*n*-butylammonium hexafluorophosphate TBAPF$_6$ and 0.01 M monor in dichloromethane solution at 100 mV s^{-1} sweep rate.
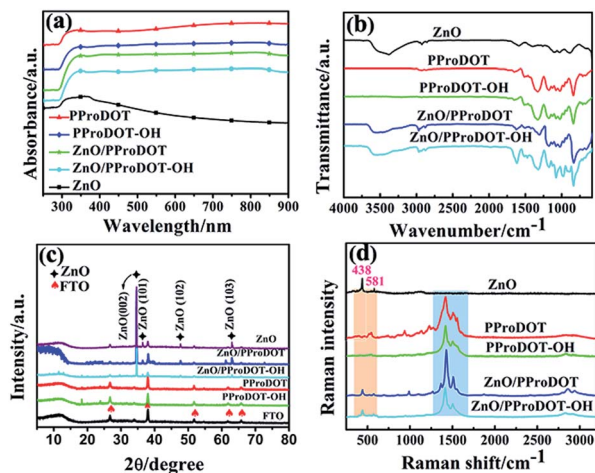
Fig. 4 (a) UV-vis, (b) FTIR, (c) XRD, (d) Raman spectra ZnO, PProDOT, PProDOT–OH, ZnO/PProDOT, ZnO/PProDOT–OH composites.

Fig. 5 Mapping images of (a) ZnO/PProDOT, (b) ZnO/ProDOT–OH composites.

Fig. 4(a). As shown in Fig. 4(a), both ZnO and ZnO/PProDOT and the ZnO/PProDOT–OH composites exhibit a ZnO band edge absorption characteristic at approximately 360–380 nm. However, the ZnO band edge absorption characteristic blue shift to near 365 nm in ZnO/PProDOT and the ZnO/PProDOT–OH composites, which is due to the quantum size effect of ZnO nanomaterials.[43] The peak of polymers and ZnO/PProDOT and ZnO/PProDOT–OH composites at 425 nm to 615 nm are attributed to the π–π* transition of the thiophene ring, and the peak above 620 nm are ascribed to the p-type doping of the polymer. Compared with the polymer, the peak corresponding to the π–π* transition of the composite is red-shifted, from 425–615 nm to 435–625 nm, which indicates that the conjugation degree of composites has increased after the composition. To compare with ZnO, the composites have absorption around the 600–900 nm, indicating that the composites can undergo electronic transitions at lower energy, which is beneficial to improving the UV responsiveness of the composites.

3.6. Fourier transform infrared spectra

The chemical structures of ZnO, PProDOT, PProDOT–OH, ZnO/PProDOT and ZnO/PProDOT–OH composites were characterized by FT-IR analysis. Fig. 4(b) shows the FT-IR spectra of ZnO, PProDOT, PProDOT–OH, ZnO/PProDOT and ZnO/PProDOT–OH composites. As shown in the spectra, ZnO found many tensile and bending vibration peaks near 3376, 2920, 1600, 1408, 870 cm^{-1}, which is attributed to the water adsorption on the surface of ZnO at room temperature.[44] These peaks can also be found in ZnO/PProDOT and ZnO/PProDOT–OH composites, which indicates that ZnO/PProDOT and ZnO/PProDOT–OH composites have been successfully prepared. PProDOT and ZnO/PProDOT showed absorption peaks at 1646, 1515, 1329, 1177, 1128, 1090, 1024, 839 and 710 cm^{-1}. Among them, the absorption peaks at 1515 cm^{-1} and 1329 cm^{-1} are the stretching vibrations of the C=C bond of the thiophene ring. The absorption peak at 1177, 1128 and 1024 cm^{-1} are the bending vibration of C–O–C. The absorption peaks at 839 cm^{-1} and 710 cm^{-1} are attributed to
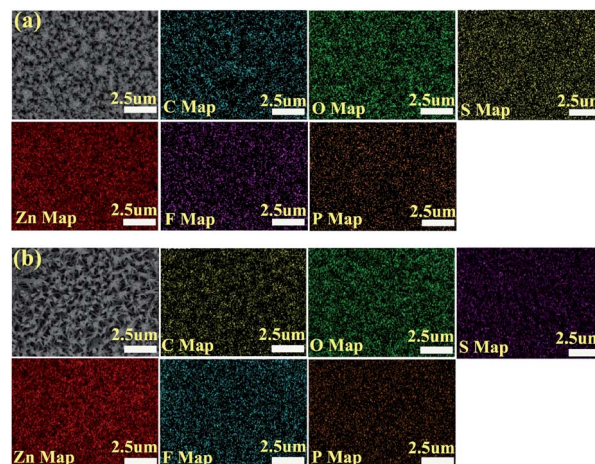
the vibration of the C–S–C bond of the PProDOT thiophene ring. PProDOT–OH and ZnO/PProDOT–OH have strong characteristic absorption peaks at 1613, 1322, 1137, 1078, 1023, 846, 702 cm^{-1}. Among them, the characteristic absorption peak at 1613 cm^{-1} and 1322 cm^{-1} belongs to the stretching vibration of C=C and C–C in the thiophene ring, while the characteristic absorption peak at 1137, 1078 and 1023 cm^{-1} attribute to the stretching vibration of C–O–C and C–S–C, respectively.[45] In a word, the characteristic bands of PProDOT and PProDOT–OH polymers are reflected in the spectra of ZnO/PProDOT and ZnO/PProDOT–OH, except for some slight changes, there is no obvious change, and no new peaks are found, which further indicates that PProDOT and PProDOT–OH polymers were successfully electrodeposited on the surface of ZnO NRs.

3.7. X-ray diffraction analysis

The phase composition of the composites was further analyzed by XRD. Fig. 4(c) presents the XRD patterns of ZnO, PProDOT, PProDOTOH, ZnO/PProDOT, and the ZnO/PProDOT–OH composites. In the figure, the XRD pattern of ZnO, ZnO/PProDOT, and ZnO/PProDOT–OH composites show several characteristic peaks possessed by ZnO, all of which can be indexed in hexagonal wurtzite ZnO (JCPDS no. 36-1451). The specific main diffraction peaks at 34.4°, 36.3°, 47.5°, and 62.9° correspond to (002), (101), (102), and (103).[46] The diffraction peak of ZnO (002) crystal plane is stronger than the diffraction peaks of ZnO (101), (102) and (103), which indicates that ZnO NRs tend to grow along the c-axis direction, which is consistent with the results of SEM. In addition, the intensity of the (002) diffraction peak is still the highest in ZnO/PProDOT and ZnO/PProDOT–OH composites, but the intensity of each diffraction peak of ZnO is lower than that of pure ZnO, which can be explained by the principle of XRD diffraction. Because the nano-film material generally chooses small-angle diffraction, the penetration of X-ray is greatly limited, while a layer of PProDOT, PProDOT–OH organic film is deposited on ZnO nanorods, so the diffraction

peak intensity of ZnO will be weakened in the ZnO/PProDOT and ZnO/PProDOT–OH composites.

3.8. Raman spectra

The Raman spectra of ZnO, PProDOT, PProDOT–OH, ZnO/PProDOT, and ZnO/PProDOT–OH composites are presented in Fig. 4(d). As shown in the figure, the Raman spectra of ZnO, ZnO/PProDOT, and the ZnO/PProDOT–OH composites, two peaks can be seen at 438 cm^{-1} and 583 cm^{-1}, which are the E_2 and A_1 (LO) modes of ZnO associated with oxygen deficiency, respectively. However, the peaks of the A_1 (TO) and E_1 (TO) modes did not appear in the Raman spectra, indicating the highly oriented growth of the ZnO NRs prepared in this study along the c axis.[47] In polymers and composites, the absorption peaks at 1504 and 1424 cm^{-1} belong to the symmetric $C_\alpha = C_\beta$ stretching of the thiophene ring in the polymer, and the absorption peaks near 1350 and 1276 cm^{-1} are attributed to the $C_\beta = C_\beta$ and $C_\alpha = C_\alpha$ inter-ring stretching of the thiophene groups in the polymer (PProDOT), respectively.[48]

3.9. Energy-dispersive spectroscopy and mapping

Fig. S3† shows the energy-dispersive X-ray spectroscopy (EDS) imaging of the ZnO/PProDOT, and ZnO/PProDOT–OH composites. The elemental mapping of Zn, O, C, and S is presented in Fig. 5. EDS analysis clearly showed that the PProDOT and PProDOT–OH polymer film was attached to the surface of the ZnO nanoarray. The elements F and P in the ZnO/PProDOT and ZnO/PProDOT–OH hybrid composites were also observed. The reason was that a certain amount of the TBAPF$_6$ electrolyte ($M = 387.43$) in the monomer solution used polymer electrodeposition.

3.10. X-ray photoelectron spectroscopy

The X-ray photoelectron spectra of ZnO, ZnO/PProDOT and ZnO/PProDOT–OH composites are shown in Fig. 6. The full spectrum of ZnO shows that the main elements on the surface of the prepared ZnO are Zn and O, and a small amount of C is adsorbed. We have carefully scanned the Zn 2p peak with the strongest signal in the whole spectrum, and it can be clearly seen from the picture that there are two peaks on 1020.28 eV and 1043.28 eV, corresponding to the difference of 23 eV between the Zn 2p$_{3/2}$ and Zn 2p$_{1/2}$, peaks of Zn^{2+} in ZnO, which is consistent with the Zn–O binding energy of ZnO reported in the literature.[49] As shown in Fig. 6(b) and (c), compared with pure ZnO, Zn 2p$_{3/2}$ and Zn 2p$_{1/2}$ in ZnO/PProDOT moved to 1020.48 eV and 1043.58 eV, while in PProDOT–OH moved to 1020.58 eV and 1043.78 eV, respectively, which may be due to the interaction between ZnO and polymer. Fig. 6(a) shows the fine scan results of the O 1s peak. According to the experimental data, the O 1s peak is obviously broadened. We further fit the O 1s peak, and the fitting results show that the observed O 1s peak consists of three parts: the low binding energy 529.88 eV peak is narrow, corresponding to the lattice oxygen atoms in zinc oxide, and the 530.68 eV is corresponding to the existence of O^{2-} near the oxygen vacancy on the surface of ZnO NRS, and the high binding energy 532.08 eV peak is wide, corresponding to the
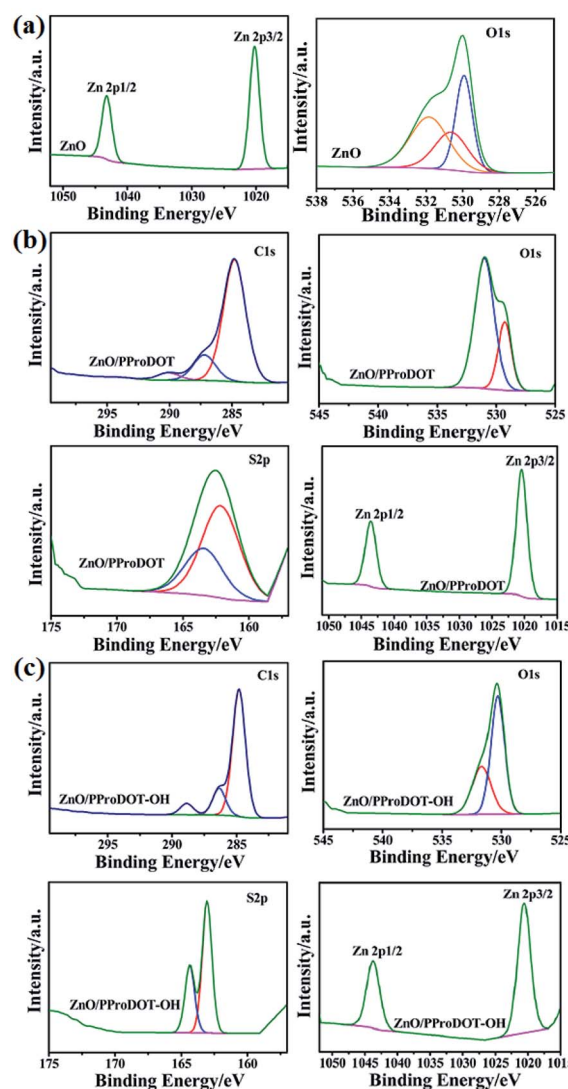

Fig. 6 XPS spectra of (a) ZnO (b) ZnO/PProDOT, (c) ZnO/ProDOT–OH composites.

oxygen adsorbed on the lattice surface. XPS signals are measured in ultra-high vacuum (less than 10^{-7} Pa). Under such high vacuum conditions, there are still oxygen molecules adsorbed on the surface of ZnO nanoarrays, so there are a large number of surface adsorbed gases in exposed air. These surface adsorbed oxygen molecules will participate in the photoelectric detection response process of ZnO NRs, which is of great significance for the subsequent analysis of the ultraviolet response process of ZnO NRs.[50]

3.11. Photoelectricity performance of composites

Fig. 7 shows the I–V behaviors of the ZnO, ZnO/PProDOT, and ZnO/PProDOT–OH composites under dark and illuminated (365 nm UV light) conditions. The UV detector fabricated from the polymer/ZnO NRs composites showed stable detection behavior and desirable properties of a rectifier, indicating that polymer deposition exerted no effect on the structure of the
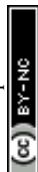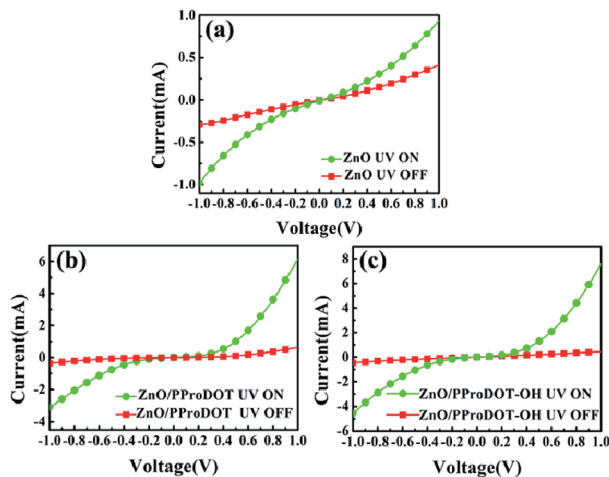

Fig. 7 I–V behaviors of (a) ZnO (b) ZnO/PProDOT, (c) ZnO/PProDOT–OH composites under the dark and 365 nm UV illumination.

device. The current of the UV detector under light conditions is markedly higher than that under dark conditions, indicating that the prepared UV detector exhibits a good response to UV. The responsivity (R) of the UV detector can be calculated using the following formula:

$$R = (I_{ph} - I_{dark})/(P \times S)$$

where I_{ph} denotes the current of the device under light conditions, I_{dark} represents the current of the device under dark conditions, P is the intensity of UV light irradiation, and S is the actual irradiation area of the device. The formula shows that R is proportional to the photogenerated current when the light irradiated area and light intensity are constant. Therefore, the R value of the device can be effectively increased by increasing the photogenerated current.

Fig. 8 presents the I–V curves of the ZnO, ZnO/PProDOT, and ZnO/PProDOT–OH composites with and without UV radiation. As shown in Fig. 8(a), the measured current of the UV detector
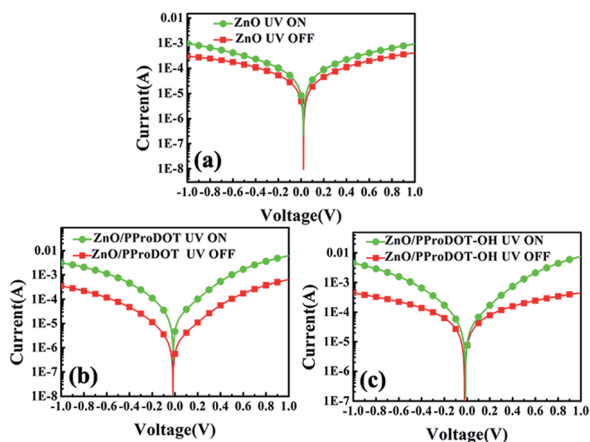
prepared using pure ZnO NRs under light conditions is significantly improved relative to that under dark conditions. The UV light responsivity of ZnO is controlled by oxygen adsorption and desorption on its surface. Without UV light irradiation, oxygen adsorption of free electrons occurs on the ZnO surface in the form of O^{2-}, leading to a decrease in ZnO conductivity by inducing the formation of a depletion region on the ZnO surface.

$$O_2(g) + e^- \rightarrow O^{2-}(ad).$$
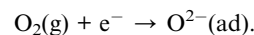
However, when exposed to UV light, the holes generated by UV radiation combine with O^{2-}, leading to oxygen desorption from the ZnO surface, and lead to an increase in the conductivity of ZnO.
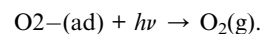
$$O2-(ad) + h\nu \rightarrow O_2(g).$$

Fig. 9 shows the time response curve of the ZnO, ZnO/PProDOT, and the ZnO/PProDOT–OH composites illuminated by UV light at 365 nm. The speed of response and recovery of the UV detector could be determined from the rise time (T_{rise}) and decay time (T_{decay}). T_{rise} denotes the time required for the photoelectric current to rise to 90% of the steady current, and T_{decay} represents the time required for the photoelectric current to fall to 10% of the steady current. The T_{rise} and T_{decay} values of the UV detector fabricated from pure ZnO were 395 and 752 s, respectively. After the deposition of the PProDOT film, the T_{rise} and T_{decay} values of the UV detector fabricated using the ZnO/PProDOT composites decreased to 174 and 370 s. The T_{rise} and T_{decay} values of the detector produced using ZnO/PProDOT–OH composites were smaller than those of the UV detector produced from ZnO/PProDOT–OH composites were 167 and 341 s, respectively. The UV photodetectors fabricated using polymer/ZnO NRs structures exhibited good photoelectric response characteristics than those of the UV photodetectors
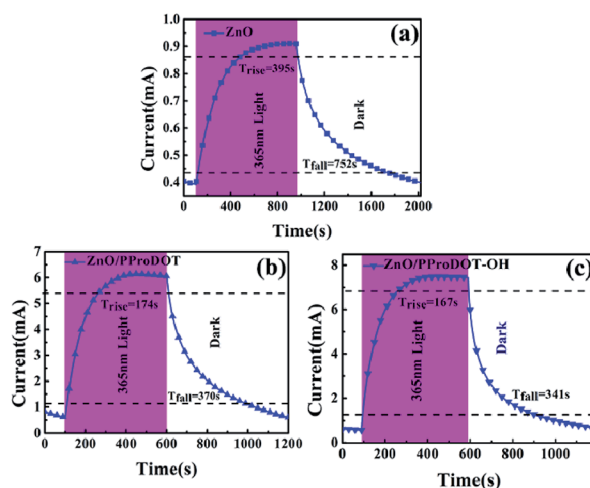

Fig. 8 I–V curves of (a) ZnO (b) ZnO/PProDOT, (c) ZnO/PProDOT–OH composites under the dark and 365 nm UV illumination.

Fig. 9 Time response curve of (a) ZnO (b) ZnO/PProDOT, (c) ZnO/PProDOT–OH composites under UV light at 1 V bias.

Table 1 Comparison of UV photo-sensing performances of the present work with previous work

Materials	Light tensity (mW cm^{-2})	λ (nm)	τ_r (s)	τ_f (s)	R (A W^{-1})	Ref.
ZnO nanoroads	0.3	365	300	500	15.6	51
ZnO microtube	21.7	365	36	>2000	6.2	52
ZnO NWs	2.3	380	55.5	33.1	0.1	53
Ga doped ZnO	—	374	95	2068	1.68	54
CuSCN/ZnO NRs	0.5	350	449	331	—	55
Porous ZnO	0.1	370	250	150	13	56
Ag/ZnO network	—	380	15	330	2.16	57
ZnO NRs	0.4	365	395	752	2.5	This work
ZnO/PProDOT	0.4	365	174	370	27.5	This work
ZnO/PProDOT–OH	0.4	365	167	341	34.75	This work

Table 2 Comparison of UV photo-sensing performances (detectivity and EQE) of the present work with previous work

Materials	Light tensity (mW cm^{-2})	λ (nm)	D^* (Jones)	EQE (%)	Ref.
ZnO/PEDOT:PSS	3	365	5.25×10^{10}	—	58
ZnO NWs	—	360	1.9×10^{8}	>100	59
ZnO thin-films	0.78	365	4.6×10^{12}	8283	60
ZnO NRs	0.4	365	2.21×10^{11}	850	This work
ZnO/PProDOT	0.4	365	1.98×10^{12}	9325	This work
ZnO/PProDOT–OH	0.4	365	2.61×10^{12}	11 780	This work

produced from pure ZnO. The enhancement could be attributed to the synergistic interaction between ZnO and polymer. The UV photosensing performances of the present study and previous reports are compared in Tables 1 and 2. Generally, the ultraviolet photodetector devices based on ZnO/polymer composites were fabricated by spin coating of polymer solutions on ZnO NRs, which needs the polymer dispersed in solvent. However, the disadvantages of above method is difficult to control the amount of polymer on ZnO NRs. This research proposes an electrochemical deposition method to prepare ZnO/polymer composites for UV photodetectors. As shown in Tables 1 and 2, UV detectors prepared by electrochemical deposition methods exhibit high UV responsiveness under 365 nm UV light irradiation. This indicates that it is feasible to prepare composite-based ultraviolet detectors by electrochemically depositing polymers on the surface of ZnO NRs.

Fig. 10 shows the time-dependent photocurrent response of UV detectors fabricated from ZnO, ZnO/PProDOT, and ZnO/PProDOT–OH composites illuminated with 365 nm UV light. As shown in Fig. 10, the prepared UV photodetectors exhibit a stable photoconductive switch behavior. Under UV radiation, the current reaches maximum saturation within a certain time and remains in this state, indicating that the prepared ZnO/polymer UV detector exhibits good stability. Oxygen adsorption in the optical gain of the ZnO surface plays an important role in light response. However, oxygen adsorption and desorption occur at relatively slow rates. Moreover, numerous defects are found on the ZnO NR surface, which can affect electron transfer and lead to a slow photoconductive process. The polymer film electrodeposited on the ZnO NRs surface may exerta partial

passivation effect on the ZnO NRs surface, greatly reducing the interaction between oxygen and the ZnO surface. A hetero-junction region is thus formed between the polymer film and the ZnO NRs surface. This heterojunction increases the bending region of the surface band and the barrier height, further improving the performance of the device.

The response time of the UV photodetector fabricated from the ZnO/PProDOT–OH composite was shorter than that of the UV photodetector prepared using the ZnO/PProDOT composite. The reason is that functional groups (–OH) can occupy the oxygen vacancy on the ZnO surface. Oxygen vacancies exist on
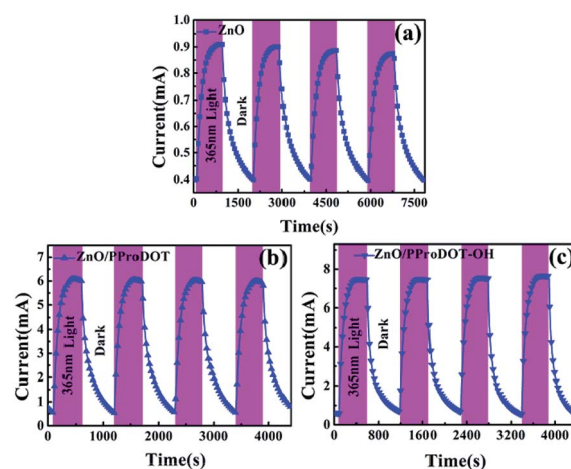

Fig. 10 Time-dependent photocurrent response of (a) ZnO (b) ZnO/PProDOT, (c) ZnO/PProDOT–OH composites under UV light at 1 V bias.

the surface of ZnO NRs synthesized using the hydrothermal method, which can reduce the available carriers in the air. The light response of the UV detector fabricated from the ZnO/polymer composite was significantly higher than that of the UV detector prepared from pure ZnO nanoarrays. The production of an oxygen defect $(O_o^\times)$ generally releases two electrons in accordance with $O_o^\times \to \frac{1}{2}O_2 + V_o^{2+} + 2e^-$.[35] The generated oxygen defect vacancy (V_o^+) is unstable and tends to stabilize by binding to the surrounding negative charges, thereby decreasing the number of free electrons in the environment. Therefore, under UV irradiation, the bonds between the oxygen defect vacancy and negative charges in the environment are broken, thereby increasing the number of free electrons on the ZnO surface. This increase markedly enhances optical response. We assume that the –OH functional groups on the PProDOT–OH polymer can form $V_o^+ - OH$ bonds on the surface of the ZnO nanostructure, thereby improving the photosensitivity of the ZnO/PProDOT–OH composite.

4. Conclusion

In summary, hydroxyl group-functionalized PProDOT/ZnO composite was prepared by electrochemical deposition method for ultraviolet photodetector, and the structure and ultraviolet photodetection properties of this composite were compared with that of ZnO/PProDOT. It is found that the composites could undergo electronic transitions at lower energy, and the coupling effect between the p-type polymers and n-type ZnO inhibited the recombination of photogenerated electrons on the surface of ZnO NRs. This could improve the response of pure ZnO to ultraviolet light. Due to the occupation of the oxygen vacancies of ZnO NRs by hydroxyl group (–OH) in PProDOT–OH, it is favor for the formation $V_o^+ - OH$ bonds on the surface of ZnO NRs after coating with PProDOT–OH. This consequently enhanced the responsiveness of UV photodetector from ZnO/PProDOT–OH composite and led the ZnO/PProDOT–OH composite displayed shorter response time than that of ZnO/PProDOT. Under UV irradiation of 365 nm, the UV photodetector from ZnO/PProDOT–OH composite showed a photoresponsivity of 34.75 A W^{-1}, which was 13 times higher than that of the UV detector fabricated from pure ZnO NRs (2.5 A W^{-1}), and was 1.26 times higher than that of ZnO/PProDOT (27.5 A W^{-1}). Compared with that of the UV photodetector based on pure ZnO NRs, the electrochemical deposition of p-type polymers significantly improved the switching ratio and light response current. With respect to the response speed, the rise time and fall time also significantly improved. The present study provides a new perspective for polymer-modified UV detection material systems to effectively improve the performance of UV photodetectors and is potentially valuable in the UV detection of polymer-modified semiconductors.

Conflicts of interest

The authors declare that there are no conflicts of interest.

Acknowledgements

References

1 L. Yang, H. Zhou, M. Xue, Z. Song and H. Wang, *Sens. Actuators, A*, 2017, **267**, 76–81.

2 S. Kim, Y. T. Lim, E. G. Soltesz, A. M. De Grand, J. Lee, A. Nakayama, J. A. Parker, T. Mihaljevic, R. G. Laurence, D. M. Dor, L. H. Cohn, M. G. Bawendi and J. V. Frangioni, *Nat. Biotechnol.*, 2004, **22**, 93–97.

3 D. Yao, W. Hao, X. Yang and Y. Tian, *Int. Symp. Photoelectron. Detect. Imaging, 2011: Adv. Imaging Detect. Appl.*, 2011, vol. 8194, p. 819436.

4 J. Lähnemann, M. Den Hertog, P. Hille, M. De La Mata, T. Fournier, J. Schörmann, J. Arbiol, M. Eickhoff and E. Monroy, *Nano Lett.*, 2016, **16**, 3260–3267.

5 J. Wei and J. Ahn, *Cryst. Res. Technol.*, 1999, **34**, 133–140.

6 X. Fang, Y. Bando, M. Liao, U. K. Gautam, C. Zhi, B. Dierre, B. Liu, T. Zhai, T. Sekiguchi, Y. Koide and D. Golberg, *Adv. Mater.*, 2009, **21**, 2034–2039.

7 C. Zhang, Y. Xie, H. Deng, T. Tumlin, C. Zhang, J. W. Su, P. Yu and J. Lin, *Small*, 2017, **13**, 1–7.

8 X. Chang, X. Qiao, K. Li, P. Wang, Y. Xiong, X. Li, F. Xia and Q. Xue, *Sens. Actuators, B*, 2020, **317**, 128208.

9 J. S. Lewis, Z. Barani, A. S. Magana and F. Kargar, *Mater. Res. Express*, 2019, **6**, 085325.

10 C. Y. Xu, L. Zhen, J. T. Jiang, C. S. Lao and L. Yang, *Ceram. Int.*, 2009, **35**, 3021–3025.

11 H. Liu, Z. Zhang, L. Hu, N. Gao, L. Sang, M. Liao, R. Ma, F. Xu and X. Fang, *Adv. Opt. Mater.*, 2014, **2**, 771–778.

12 Ü. Özgür, Y. I. Alivov, C. Liu, A. Teke, M. A. Reshchikov, S. Doğan, V. Avrutin, S. J. Cho and H. Morko, *J. Appl. Phys.*, 2005, **98**, 1–103.

13 Z. L. Wang, *Mater. Sci. Eng., R*, 2009, **64**, 33–71.

14 X. L. Zhang, K. S. Hui and K. N. Hui, *Mater. Res. Bull.*, 2013, **48**, 305–309.

15 Y. He, W. Zhang, S. Zhang, X. Kang, W. Peng and Y. Xu, *Sens. Actuators, A*, 2012, **181**, 6–12.

16 D. Basak, G. Amin, B. Mallik, G. K. Paul and S. K. Sen, *J. Cryst. Growth*, 2003, **256**, 73–77.

17 H. Ohta, M. Kamiya, T. Kamiya, M. Hirano and H. Hosono, *Thin Solid Films*, 2003, **445**, 317–321.

18 Y. Li, F. Della Valle, M. Simonnet, I. Yamada and J. J. Delaunay, *Nanotechnology*, 2009, **20**, 045501.

19 H. J. Yuan, S. S. Xie, D. F. Liu, X. Q. Yan, Z. P. Zhou, L. J. Ci, J. X. Wang, Y. Gao, L. Song, L. F. Liu, W. Y. Zhou and G. Wang, *Chem. Phys. Lett.*, 2003, **371**, 337–341.

20 B. D. Yao, Y. F. Chan and N. Wang, *Appl. Phys. Lett.*, 2002, **81**, 757–759.

21 Z. L. Wang, X. Y. Kong, Y. Ding, P. Gao, W. L. Hughes, R. Yang and Y. Zhang, *Adv. Funct. Mater.*, 2004, **14**, 943–956.

22 H. Y. Lu, S. Y. Chu and S. H. Cheng, *J. Cryst. Growth*, 2005, **274**, 506–511.

23 X. Q. Meng, D. Z. Shen, J. Y. Zhang, D. X. Zhao, Y. M. Lu, L. Dong, Z. Z. Zhang, Y. C. Liu and X. W. Fan, *Solid State Commun.*, 2005, **135**, 179–182.

24 W. Tian, T. Zhai, C. Zhang, S. L. Li, X. Wang, F. Liu, D. Liu, X. Cai, K. Tsukagoshi, D. Golberg and Y. Bando, *Adv. Mater.*, 2013, **25**, 4625–4630.

25 A. Echresh, C. O. Chey, M. Zargar Shoushtari, V. Khranovskyy, O. Nur and M. Willander, *J. Alloys Compd.*, 2015, **632**, 165–171.

26 C. W. Na, H. S. Woo and J. H. Lee, *RSC Adv.*, 2012, **2**, 414–417.

27 Y. Yang, W. Guo, J. Qi, J. Zhao and Y. Zhang, *Appl. Phys. Lett.*, 2010, **97**, 44–47.

28 M.-W. Chen, C.-Y. Chen, D.-H. Lien, Y. Ding and J.-H. He, *Opt. Express*, 2010, **18**, 14836.

29 S. Patra, A. Ray, A. Roy, P. Sadhukhan, S. Pujaru, U. K. Ghorai, R. Bhar and S. Das, *Mater. Res. Bull.*, 2018, **101**, 240–245.

30 Y. Q. Bie, Z. M. Liao, H. Z. Zhang, G. R. Li, Y. Ye, Y. B. Zhou, J. Xu, Z. X. Qin, L. Dai and D. P. Yu, *Adv. Mater.*, 2011, **23**, 649–653.

31 S. L. Chang, M. C. Park, Q. Kuang, Y. Deng, A. K. Sood, D. L. Polla and Z. L. Wang, *J. Am. Chem. Soc.*, 2007, **129**, 12096–12097.

32 S. Yang, J. Gong and Y. Deng, *J. Mater. Chem.*, 2012, **22**, 13899–13902.

33 M. Nakano, A. Tsukazaki, R. Y. Gunji, K. Ueno, A. Ohtomo, T. Fukumura and M. Kawasaki, *Appl. Phys. Lett.*, 2007, **91**, 1–4.

34 X. Yang, S. Seo, C. Park and E. Kim, *Macromolecules*, 2014, **47**, 7043–7051.

35 N. Chantarat, Y. W. Chen, S. Y. Chen and C. C. Lin, *Nanotechnology*, 2009, **20**, 395201.

36 Y. C. Yoon, K. S. Park and S. D. Kim, *Thin Solid Films*, 2015, **597**, 125–130.

37 B. D. Reeves, E. Unur, N. Ananthakrishnan and J. R. Reynolds, *Macromolecules*, 2007, **40**, 5344–5352.

38 J. Heinze, A. Rasche, M. Pagels and B. Geschke, *J. Phys. Chem. B*, 2007, **111**, 989–997.

39 E. M. Genies, G. Bidan and A. F. Diaz, *J. Electroanal. Chem.*, 1983, **149**, 101–113.

40 A. Diaz, *J. Electroanal. Chem.*, 1981, **129**, 115–132.

41 N. Sakmeche, S. Aeiyach, J. J. Aaron, M. Jouini, J. C. Lacroix and P. C. Lacaze, *Langmuir*, 1999, **15**, 2566–2574.

42 K. Manivannan, M. Sivakumar, C. C. Cheng, C. H. Lu and J. K. Chen, *Sens. Actuators, B*, 2019, **301**, 1–8.

43 S. Fujihara, H. Naito and T. Kimura, *Thin Solid Films*, 2001, **389**, 227–232.

44 R. Ghosh, S. Kundu, R. Majumder, S. Roy, S. Das, A. Banerjee, U. Guria, M. Banerjee, M. K. Bera, K. M. Subhedar and M. P. Chowdhury, *Appl. Nanosci.*, 2019, **9**, 1939–1952.

45 R. Jamal, L. Zhang, M. Wang, Q. Zhao and T. Abdiryim, *Prog. Nat. Sci.: Mater. Int.*, 2016, **26**, 32–40.

46 A. Katiyar, N. Kumar and A. Srivastava, *Mater. Today: Proc.*, 2018, **5**, 9144–9147.

47 A. P. de Moura, R. C. Lima, M. L. Moreira, D. P. Volanti, J. W. M. Espinosa, M. O. Orlandi, P. S. Pizani, J. A. Varela and E. Longo, *Solid State Ionics*, 2010, **181**, 775–780.

48 P. Damlin, M. Suominen, M. Heinonen and C. Kvarnström, *Carbon*, 2015, **93**, 533–543.

49 N. M. Vuong, N. D. Chinh, B. T. Huy and Y. I. Lee, *Sci. Rep.*, 2016, **6**, 26736.

50 C. Wei, J. Xu, S. Shi, R. Cao, J. Chen, H. Dong, X. Zhang, S. Yin and L. Li, *J. Mater. Chem. C*, 2019, **7**, 9369–9379.

51 Y. Li, X. Dong, C. Cheng, X. Zhou, P. Zhang, J. Gao and H. Zhang, *Phys. Rev. B: Condens. Matter Mater. Phys.*, 2009, **404**, 4282–4285.

52 J. Cheng, Y. Zhang and R. Guo, *J. Cryst. Growth*, 2008, **310**, 57–61.

53 S. H. Lee, S. H. Kim and J. S. Yu, *Nanoscale Res. Lett.*, 2016, **11**, 333.

54 L. J. Mandalapu, F. X. Xiu, Z. Yang and J. L. Liu, *Solid-State Electron.*, 2007, **51**, 1014–1017.

55 S. Li, J. Xu, S. Shi, X. Shi, X. Wang, C. Wang, X. Zhang, Z. Liu and L. Li, *Chem. Phys. Lett.*, 2015, **620**, 50–55.

56 N. Nasiri, R. Bo, F. Wang, L. Fu and A. Tricoli, *Adv. Mater.*, 2015, **27**, 4336–4343.

57 X. Wang, K. Liu, X. Chen, B. Li, M. Jiang, Z. Zhang, H. Zhao and D. Shen, *ACS Appl. Mater. Interfaces*, 2017, **9**, 5574–5579.

58 B. Deka Boruah and A. Misra, *ACS Appl. Mater. Interfaces*, 2016, **8**, 18182–18188.

59 W. Y. Weng, S. J. Chang, C. L. Hsu, T. J. Hsueh and S. P. Chang, *J. Electrochem. Soc.*, 2010, **157**, K30.

60 M. A. Khan, M. K. Singha, K. K. Nanda and S. B. Krupanidhi, *Appl. Surf. Sci.*, 2020, **505**, 144365.